An Efficiency Optimization-Based Asymmetric Tuning Method of Double-Sided *LCC* Compensated WPT System for Electric Vehicles

Yafei Chen, *Student Member, IEEE*, Hailong Zhang, *Student Member, IEEE*, Chang-Su Shin, Cheol-Hee Jo, Sung-Jun Park, *Member, IEEE*, and Dong-Hee Kim, *Member, IEEE*

***Abstract*—Compensation topologies play an essential role in wireless power transfer systems for electric vehicles. Specifically, the double-sided *LCC* compensated (DS-*LCC*) topology has been widely adopted, owing to its inherent advantages, such as load-independent constant current (CC) output, low sensitivity to load variation, and high freedom in parameter design. However, large resonant devices in the DS-*LCC* topology lower the system efficiency and increase the complexity of optimal parameter tuning. Therefore, in this article, the parameters of the DS-*LCC* compensation topology are reconfigured by adjusting the ratios of its two compensation inductances without changing the specified system-level parameters, such as the loosely coupled transformer, operating frequency, and specified CC outputs. The system performance under each case is analyzed and compared in detail, based on which, an asymmetric parameter-design method is proposed to optimize the system efficiency. To verify the reasonability of the proposed tuning method, a 6.6-kW experimental prototype is configured, and comparative experiments are conducted. The experimental results indicate that, compared with the conventional method, the proposed parameter-tuning method improves the system efficiency under overall load conditions, especially under light loads.**

***Index Terms*—Double-sided *LCC* (DS-*LCC*) compensation topology, efficiency optimization, electric vehicles (EVs), parameter-design method, wireless power transfer (WPT).**

I. Introduction

IN THE backdrop of continuous global fossil energy depletion and environmental deterioration, electric vehicles (EVs) are being developed for environmental protection, energy efficiency, and to reduce carbon footprint [1]. Wireless power transfer (WPT), also called inductive power transfer, is a novel and alternative technology for EV charging. Compared with the conventional contact power transfer methods, the WPT technology has gained increasing attention, and has a promising market because of its inherent advantages of convenience, reliability, lack of mechanical wear, and being weatherproof [2]–[4]. In addition to EV charging, WPT has been used in applications including unmanned aerial vehicles (UAVs), consumer electronics (CEs), and biomedical implants [5], [6].

Thus, the combination of the EV and WPT technology has extensive potential and commercial applications. However, some targeted studies are required not only to implement the mature application but also for the enormous promotion of EV wireless charging [7]. Currently, popular research topics in this field include optimal design of a loosely coupled transformer (LCT) to achieve a high coupling coefficient and misalignment tolerance [8], [9], compensation topologies with constant outputs (current or voltage) and zero phase angle (ZPA) characteristics [10]–[12], control methods for maximum efficiency tracking [13], [14], foreign-object detection, and interoperability of the charging system. Among these, compensation topology can significantly minimize the volt–ampere (VA) rating of the power supply, improve the power-transfer capability, and help achieve high efficiencies [15], [16].

Presently, four basic compensation topologies are being studied, namely the SS, SP, PS, and PP, which are mature and complete [4], [17]. Therefore, to improve the performance of the compensation network, many researchers have focused their attention on the advantageous high-order compensation topologies. For instance, Hou *et al.* [18] presented the impedance conditions and output current characteristics of different current-fed compensation topologies; they analyzed and compared the sensitivities of the output current to parameter variation. Interestingly, Lu *et al.* [19] analyzed the resonant conditions of all voltage-fed compensation topologies in a WPT system to achieve a constant-voltage (CV) output and investigated the parameters' impact on the key performance factors of these composite topologies. Among the existing high-order compensation topologies, the double-sided *LCC* topology (DS-*LCC*) is most popular because it combines all the benefits of series and parallel compensations in both the primary and secondary sides [15], [18], [20]. Therefore, this novel topology, which is composed of an inductor and two capacitors on each side, has been drawing extensive attention.

Manuscript received December 16, 2019; revised February 14, 2020; accepted March 26, 2020. Date of publication April 2, 2020; date of current version July 20, 2020. This work was supported in part by the Korea Institute of Energy Technology Evaluation and Planning (KETEP) and in part by the Ministry of Trade, Industry and Energy (MOTIE) of the Republic of Korea under Grant 20193810100001B. Recommended for publication by Associate Editor S. Williamson. *(Corresponding author: Dong-Hee Kim.)*

The authors are with the Department of Electrical Engineering, Chonnam National University, Gwangju 61186, South Korea (e-mail: swjtuqust@163.com; hailong9925@gmail.com; 198101@jnu.ac.kr; 197597@jnu.ac.kr; sjpark1@jnu.ac.kr; kimdonghee@jnu.ac.kr).

Color versions of one or more of the figures in this article are available online at http://ieeexplore.ieee.org.

Digital Object Identifier 10.1109/TPEL.2020.2984712

Moreover, owing to its massive configurable parameters, the resonant conditions in the DS-*LCC* compensation topology become irrelevant to the LCT [1] and increase the parametric design freedom. However, these massive devices also increase the complexity of parameter tuning. Li *et al.* [21] first proposed the DS-*LCC* topology and reported an original parameter-tuning method. Under the premise that the LCT parameters, dc-link voltage, constant current (CC) output, and frequency have been specified; the two compensation inductances on both sides were symmetrically designed according to these specified system parameters. Subsequently, all the compensation capacitances of the DS-*LCC* topology were determined according to the resonant conditions. This symmetric tuning method can be used to achieve the CC output and ZPA, which are independent of the load conditions. As this tuning method provides a simple design, it has been widely utilized in many studies [5], [15], [22]–[25]. Unfortunately, however, this symmetric tuning method is not sufficiently ideal for the following reasons. First, compared with some other compensation topologies with CC output characteristics such as the SS and *LCC*-P, it is more difficult to achieve a high efficiency using the DS-*LCC* system, owing to its large number of components [15], [18]. As a result, an efficiency optimization-based tuning method is more crucial for the DS-*LCC* topology, which has not been considered in the symmetric tuning method. Second, although the DS-*LCC* system has a completely symmetric topology structure on the primary (transmitter) and secondary (receiver) sides, the practical situation is quite different, especially in EV wireless charging systems. This is because the transmitter is placed underground and the receiver is mounted at the bottom of EV, and hence the rated volumes, magnetic field distributions, and voltage (current) stresses on both sides are different, which should be separately considered. Moreover, in a vehicle-to-grid WPT system, which is a topic of recent interest, a flexible tuning method-based DS-*LCC* topology is required for this bidirectional charging application.

In practice, all the compensation capacitances of the DS-*LCC* topology can be calculated according to the definite resonant conditions and specified system-level parameters, as long as the two compensation inductances are determined. Therefore, the parameter-tuning process is essentially the determination of the two compensation inductances in the DS-*LCC* topology. However, to date, related research is still scarce. Takeda *et al.* [26] proposed an asymmetric parameter design for the DS-*LCC* topology to satisfy the tradeoff between high efficiency and high output power. Because the DS-*LCC* and *LCC*-S have an identical structure on the primary side, an optimal primary compensation inductance was first selected via an *LCC*-S model, and then the optimal secondary compensation inductance of the DS-*LCC* was determined according to the optimal equivalent load. However, the CC output of the DS-*LCC* was different in the process of analysis and comparison. Therefore, the fairness of the comparison is questionable. Furthermore, while the proposed optimal parameter design was verified using a 10-W experimental prototype, the validity and feasibility of this tuning method in high-power charging systems remains unclear. Liao *et al.* [27] investigated the relationship between impedance matching and transfer efficiency under a rectifier load in the DS-*LCC* WPT system and proposed a parameter-design method for the DS-*LCC* to achieve maximum transfer efficiency. The secondary compensation inductance was chosen according to the optimum equivalent output impedance of the rectifier; however, the primary compensation inductance was designed according to the conventional design method proposed in [21]. In other words, only the secondary-side parameters of the DS–*LCC* were optimized. Furthermore, although a 3.3-kW prototype was constructed to verify the proposed tuning method, only the copper loss of the LCT was considered in the efficiency analysis. However, for a 3.3-kW WPT system, iron loss of the LCT should be considered while calculating the loss. In some other studies on the DS-*LCC* topology, the two compensation inductances were designed to be different. Nevertheless, almost no detailed design criteria for the two inductances have been provided in these studies.

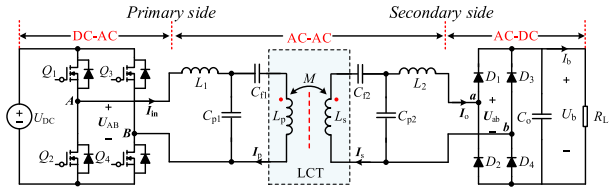

Fig. 1. DS-*LCC* compensated WPT system for EV charging.

Therefore, in this article, which is based on the symmetric tuning method proposed in [21], two identical compensation inductances of the DS-*LCC* are first established according to the essential parameters of the WPT system. Without changing the specified system-level parameters, the resonant network is reconfigured by adjusting the ratio of the two compensation inductances of the DS-*LCC* topology. Under these different combinations, the system characteristics such as voltage (current) stress, high-frequency response, as well as power loss are synthetically investigated and compared to determine an optimal ratio of the compensation inductances, which can enhance the WPT system efficiency in the entire load range. Meanwhile, an efficiency optimization-based asymmetric tuning method of the DS-*LCC* topology is also proposed for general applications. The presented analysis as well as the tuning method are validated using a 6.6-kW experimental prototype.

II. Asymmetrical Analysis and Comparison of the DS-LCC Compensated WPT System

A. Analysis Outline of the DS-LCC Compensation Topology

A schematic diagram of a DS-*LCC* compensated WPT system is shown in Fig. 1. A full-bridge inverter (FBI), which comprises four power MOSFETs Q_1-Q_4, is utilized to convert a dc-link voltage $U_{\rm DC}$ to an ac square-wave voltage $\boldsymbol{U}_{\rm AB}$. In the WPT system, the fundamental harmonic analysis (FHA) method is widely used for qualitative analysis because the resonant network suppresses the harmonics [2]. Therefore, the relational expression of $\boldsymbol{U}_{\rm AB}$ and $U_{\rm DC}$ can be derived as

$$\boldsymbol{U}_{\rm AB} = \frac{4U_{\rm DC}}{\pi}\sin(\omega t)\sin\left(\frac{\pi D}{2}\right) \tag{1}$$

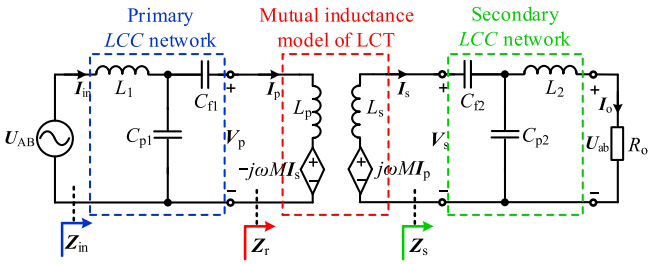

Fig. 2. Mutual-inductance model-based analytical circuit of the DS-*LCC* compensation topology.

where D is the duty cycle of $\boldsymbol{U}_{\mathrm{AB}}$ under a pulsewidth modulation control. The LCT has a primary and secondary coil and the power is transferred via the pair of coils; L_p and L_s are the self-inductances; and M is the mutual inductance between the two coils. The coupling coefficient of the LCT is defined as

$$k = \frac{M}{\sqrt{L_p L_s}}. \tag{2}$$

Two inductors, L_1 and L_2, and four capacitors C_{p1}, C_{f1}, C_{p2}, and C_{f2}, comprise the resonant networks. A bridge rectifier (BR) comprising four diodes D_1-D_4 is used to regulate the ac output voltage $\boldsymbol{U}_{ab}$ to the battery-charging voltage U_b; $\boldsymbol{I}_o$ and I_b are the corresponding ac output current and battery charging current, respectively; R_L is the dc output load; and C_o is the output filter capacitor.

When the output low-pass filter is only made up of a dc capacitor, the following equations can be derived [28]:

$$\begin{cases} U_b = \frac{\pi\sqrt{2}}{4} U_{ab} \\ I_b = \frac{2\sqrt{2}}{\pi} I_o \end{cases} \tag{3}$$

where U_{ab} and I_o are the rms values of $\boldsymbol{U}_{ab}$ and $\boldsymbol{I}_o$, respectively. Based on (3), the relational expression between R_L and R_o can be deduced as

$$R_o = \frac{8}{\pi^2} R_L. \tag{4}$$

Therefore, according to (1) and (3), the FBI and BR in Fig. 1 can be replaced by a sinusoidal voltage source and an ac equivalent load, respectively. Meanwhile, the primary and secondary coils can be decoupled using a mutual-inductance model of the LCT. Thus, the circuit in Fig. 1 can be simplified, as shown in Fig. 2. Note that the equivalent series resistances (ESRs) of the primary and secondary coils are omitted here to simplify the analyses and calculations.

According to Kirchhoff's voltage and current laws, the relational expressions between the currents and voltages can be derived as shown in (5) at the bottom of this page.

The resonant conditions of the DS-*LCC* compensation topology are expressed as follows:

$$\omega_0{}^2 L_1 C_{p1} = \omega_0{}^2 L_2 C_{p2} = 1 \tag{6}$$

$$\omega_0{}^2 (L_p - L_1) C_{f1} = \omega_0{}^2 (L_s - L_2) C_{f2} = 1. \tag{7}$$

In the above equations, ω_0 is the resonant angular frequency. The function of (6) is to achieve a load-independent CC output, and that of (7) is to implement a ZPA [21].

Under ideal conditions, according to the law of conservation of energy, the average power, which is transferred from FBI to BR, is not attenuated; this implies that

$$P_{in} = P_o = U_{\mathrm{AB}} I_{in} = U_{ab} I_o \tag{8}$$

where P_{in} and P_o, respectively, represent the input and output average power, and U_{AB} and I_{in} are the rms values of $\boldsymbol{U}_{\mathrm{AB}}$ and $\boldsymbol{I}_{\mathrm{in}}$, respectively.

When the system operates at the resonant frequency, the equations of the power transfer current group presented in (5) are derived by substituting (6), (7), and (8) into (5) and solving the matrix equations, as follows:

$$\boldsymbol{I}_{in} = \frac{M^2 \boldsymbol{U}_{\mathrm{AB}} R_o}{\omega_0{}^2 L_1{}^2 L_2{}^2} = \frac{M^2 U_{\mathrm{AB}} R_o}{\omega_0{}^2 L_1{}^2 L_2{}^2} \angle 0^\circ \tag{9}$$

$$\boldsymbol{I}_p = \frac{\boldsymbol{U}_{\mathrm{AB}}}{j\omega_0 L_1} = \frac{U_{\mathrm{AB}}}{\omega_0 L_1} \angle -90^\circ \tag{10}$$

$$\boldsymbol{I}_s = \frac{M \boldsymbol{U}_{\mathrm{AB}} R_o}{\omega_0{}^2 L_1 L_2{}^2} = \frac{M U_{\mathrm{AB}} R_o}{\omega_0{}^2 L_1 L_2{}^2} \angle 0^\circ \tag{11}$$

$$\boldsymbol{I}_o = \frac{M \boldsymbol{U}_{\mathrm{AB}}}{j\omega_0 L_1 L_2} = \frac{M U_{\mathrm{AB}}}{\omega_0 L_1 L_2} \angle -90^\circ. \tag{12}$$

Based on (9), (8) can be modified as

$$P_{in} = P_o = \frac{M^2 U_{\mathrm{AB}}{}^2 R_o}{\omega_0{}^2 L_1{}^2 L_2{}^2}. \tag{13}$$

As mentioned above, the parameter-tuning process of the DS-*LCC* topology generally involves two steps: in the first step, both the compensation inductances L_1 and L_2 are designed according to the desired CC output I_o as well as the rated output power P_o. Then, in the second step, all the compensation capacitances are determined according to the resonant conditions given by (6) and (7). In the conventional symmetric tuning method, L_1 and L_2 are designed as reported in [21]

$$L_1 = L_2 = L' = \sqrt{\frac{4kU_{\mathrm{DC}}}{\pi\omega_0}} \sqrt{\frac{L_p L_s R_o}{P_o}}. \tag{14}$$

Equation (14) indicates that L_1 and L_2 are uniquely determined as L' as long as the system's essential parameters are invariable. However, high design freedom, which is the most significant advantage of the DS-*LCC* topology, is not completely

$$\begin{bmatrix} j\omega L_1 + \frac{1}{j\omega C_{p1}} & -\frac{1}{j\omega C_{p1}} & 0 & 0 \\ -\frac{1}{j\omega C_{p1}} & j\omega L_p + \frac{1}{j\omega C_{p1}} + \frac{1}{j\omega C_{f1}} & -j\omega M & 0 \\ 0 & -j\omega M & j\omega L_s + \frac{1}{j\omega C_{p2}} + \frac{1}{j\omega C_{f2}} & 0 \\ 0 & 0 & \frac{1}{j\omega C_{p2}} & -j\omega L_2 - \frac{1}{j\omega C_{p2}} \end{bmatrix} \cdot \begin{bmatrix} \boldsymbol{I}_{in} \\ \boldsymbol{I}_p \\ \boldsymbol{I}_s \\ \boldsymbol{I}_o \end{bmatrix} = \begin{bmatrix} \boldsymbol{U}_{\mathrm{AB}} \\ 0 \\ 0 \\ \boldsymbol{U}_{ab} \end{bmatrix} \tag{5}$$

exploited in this case. Furthermore, the symmetric inductance L' is not usually the best choice.

The product of L_1 and L_2 is defined as

$$\sigma = L_1 L_2 = L'^2. \tag{15}$$

Based on (15), (12), and (13) can be modified as follows:

$$\boldsymbol{I}_o = \frac{M\boldsymbol{U}_{\mathrm{AB}}}{j\omega_0\sigma} = \frac{MU_{\mathrm{AB}}}{\omega_0\sigma}\angle{-90^\circ} \tag{16}$$

$$P_{in} = P_o = \frac{M^2 {U_{\mathrm{AB}}}^2 R_o}{{\omega_0}^2\sigma^2}. \tag{17}$$

Therefore, theoretically, under the premise that the essential parameters of the WPT system are constants, the specified parameters I_o, P_{in}, and P_o remain constant as long as σ remains constant. Hence, by maintaining a constant σ (i.e., the specified system parameters are constants), L_1 and L_2 can be reconfigured as follows, by changing their ratios:

$$L_1 = \gamma L' \tag{18}$$

$$L_2 = \frac{1}{\gamma} L'. \tag{19}$$

In the above equations, γ is an adjustable coefficient that indicates the degree of deviation from the symmetric inductance L'. In practice, based on the previous analysis, and combining (15)–(19), it can be determined that each γ corresponds to a different set of topology parameters. Thus, the DS-*LCC* resonant network can be reconfigured by adjusting the value of γ without changing the essential system-level parameters. The subsequent sections present the WPT system characteristics under different γ values, as well as a detailed discussion on the selection principles for determining an optimal γ.

B. Voltage and Current Stresses on the Components

The voltage as well as current stresses on the resonant components are essential considerations while analyzing a compensation technology because the excessive voltage and current stresses may increase the power loss and cause damage to the devices.

By substituting (18) and (19) into the basic expressions related to the voltage and current stress such as (9)–(12), and holding all parameters constant except γ, we see that the voltage and current stress of DS-*LCC* are only affected by γ. Therefore, to investigate the relationship between the stress of the components and γ, a set of essential system parameters were chosen, as listed in Table I, which are designed to fulfill the WPT 2 power class (7.7 kVA) of SAE J2954 recommended practice [29]. In addition, to ensure fairness of the following analysis and comparisons, the abovementioned parameters will be held constant in the subsequent analysis except where specifically mentioned.

According to the previous analysis, the symmetric inductance L' corresponds to $\gamma = 1$. Using the parameters listed in Table I and using (14) and (15), the symmetric inductance L' and the constant product σ can be calculated as 13.23 μH and 175.03 $\mu\mathrm{H}^2$, respectively. Furthermore, two different γ values on either side of $\gamma = 1$ also were selected for comparison and investigation of the variation trends of the stresses under different γ values, namely at $\gamma = 0.8$ and 1.25.

TABLE I
ESSENTIAL PARAMETERS OF THE WPT SYSTEM

Symbols	Parameters	Values
U_{DC}	DC-link input voltage	380 V
f_0	Operation frequency	85 kHz
P_{o}	Output power rating	6.6 kW
U_{b}	Charging voltage	280–420 V
I_{b}	Charging current	21.6 A
k	Coupling coefficient	0.164
L_{p}	Primary coil inductance	40 μH
L_{s}	Secondary coil inductance	40 μH

TABLE II
CALCULATED RECONFIGURABLE PARAMETERS OF THE DS-*LCC* COMPENSATION TOPOLOGY

Parameters	Values		
	$\gamma = 0.8$	$\gamma = 1.0$	$\gamma = 1.25$
L_1 (μH)	10.58	13.23	16.54
L_2 (μH)	16.54	13.23	10.58
C_{p1} (nF)	331.26	265.01	212.01
C_{p2} (nF)	212.01	265.01	331.26
C_{f1} (nF)	119.18	130.96	149.42
C_{f2} (nF)	149.42	130.96	119.18

Furthermore, we used the essential system parameters listed in Table I to operate the system in a resonant state, and the compensation capacitances corresponding to the three selected γ values were calculated according to (6) and (7). The parameters of the DS-*LCC* compensation topology under different γ values are listed in Table II. Using these parameters, the voltage and current stresses of the DS-*LCC* topology under resonant conditions were calculated and compared, as shown in Fig. 3. With regard to the current stresses, at the same output power levels (load conditions), the currents I_{L1} (I_{in}) and I_{L2} (I_o) corresponding to different γ values remain unchanged, i.e., these are independent of γ. As mentioned earlier, this is the basis of a fair comparison. The primary coil current I_p is constant and irrelevant to the output power, which is the basic feature of the DS-*LCC* topology, while the currents I_{L1}, I_s, I_{Cp1}, and I_{Cp2} increase with increasing output power. Besides, under the same output power, as γ increases, I_p and I_{Cp1} decrease while I_s and I_{Cp2} increase; this variation trend is reversed when γ decreases.

A significant observation from Fig. 3(a) is that when the other parameters are held constant, I_p and I_s can be flexibly adjusted by changing the value of γ; this variation trend is clearly shown in Fig. 4. Generally, the LCT is the most important component of the WPT system, as it significantly impacts the power transfer efficiency. Furthermore, I_p as well as I_s directly determine the power loss of the LCT, which significantly contribute to total system loss [4]. Therefore, the above analysis indicates that the power loss can be reduced by a reasonable selection of the γ value. The specific analyses of the power losses under different γ values will be discussed in the following sections.

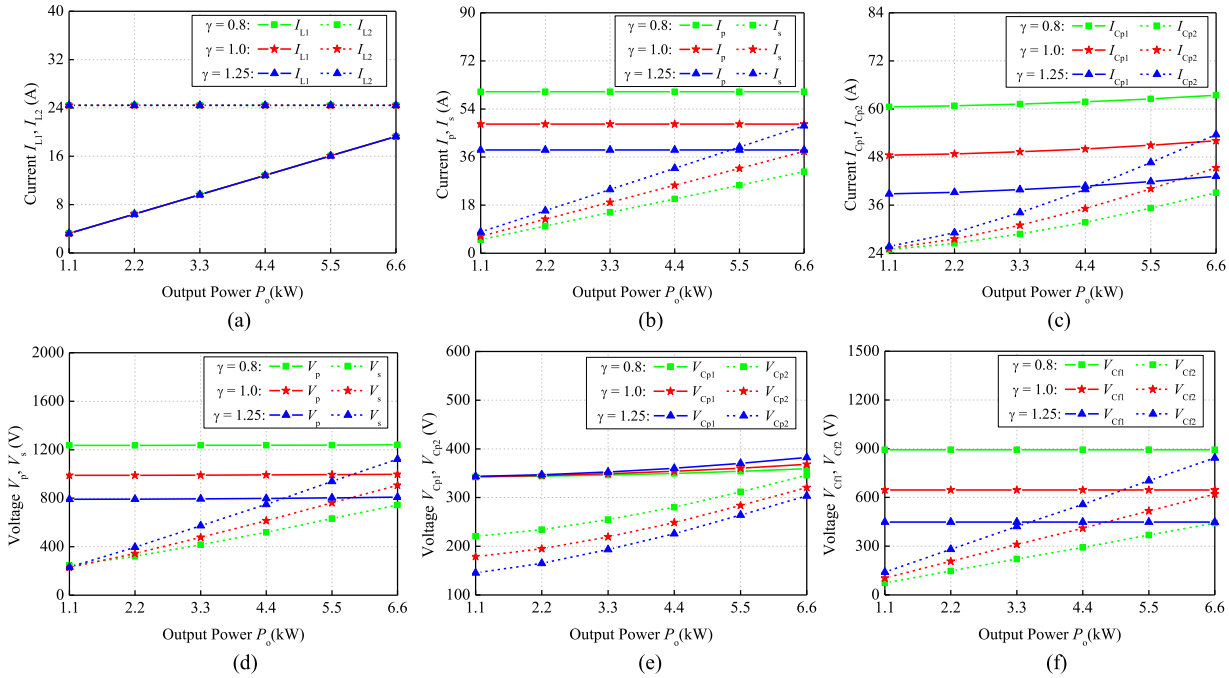

Fig. 3. Component stresses (rms values) of the DS-*LCC* topology versus P_o under different γ values for: (a) I_{L1} and I_{L2}. (b) I_p and I_s. (c) I_{Cp1} and I_{Cp2}. (d) V_p and V_s. (e) V_{Cp1} and V_{Cp2}. (f) V_{Cf1} and V_{Cf2}.

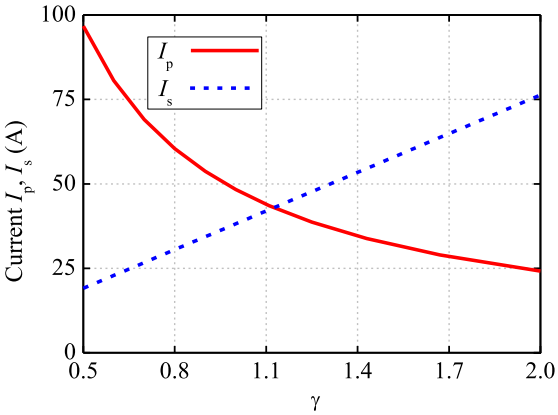

Fig. 4. Calculated I_p and I_s versus γ at 6.6-kW output power.

Fig. 3(b) shows that V_p and V_{Cf1} are nearly constant as the output power sharply increases, while V_s, V_{Cp1}, V_{Cp2}, and V_{Cf2} show an increasing trend. Furthermore, at constant output power, the voltage stresses on the resonant components would either increase or decrease with the changes in γ. In high-power WPT applications, considering that the capacitor tanks are composed of series or parallel connections of a single capacitor, and each single capacitor has its rated voltage, excessive voltage may increase the quantities of the single capacitor. Hence, in contrast to the coil voltages, more attention should be paid to the voltages of the capacitors. As shown in Fig. 3(b), the voltages on C_{p1} and C_{p2} are insensitive to γ, whereas those on C_{f1} and C_{f2} vary rapidly with the variations in γ. Moreover, an extreme selection of γ value can even cause a partial overvoltage on C_{f1} or C_{f2}.

In addition, for the tuning method discussed in this article, we assume that the parameters of the LCT have been designed, i.e., the volumes of the primary and secondary coils have been determined. Therefore, the rated I_p as well as I_s are limited by the diameters of coils. In view of this, during the parameter-tuning process, the possible value range of γ should be selected according to the rated I_p and I_s.

C. High-Order Harmonic Suppression (HHS)

As discussed in the previous section, a prominent function of the compensation topologies is to compensate the large leakage inductances of the LCT. Furthermore, because the resonant networks are made up of inductors and capacitors, the compensation topologies can work as a passive bandpass filter, which only allows the specified resonant-frequency component to pass. As a result, the harmonic components can be significantly attenuated [30]. Nonetheless, owing to its large number of resonant components, the DS-*LCC* compensation topology has many self-resonant frequencies, and therefore, its HHS ability is not outstanding.

Normally, the loss on the switches can be greatly increased by the high-order harmonics [21]. In addition, the FHA method, which is widely adopted in the WPT systems, is an approximate calculation method: when the WPT system is analyzed and calculated by this method, only the fundamental components are considered, while the harmonics are ignored. Therefore, the harmonics can considerably increase the deviations between the design and the practical values. In this section, the HHS performance of the DS-*LCC* under different γ values is compared and investigated.

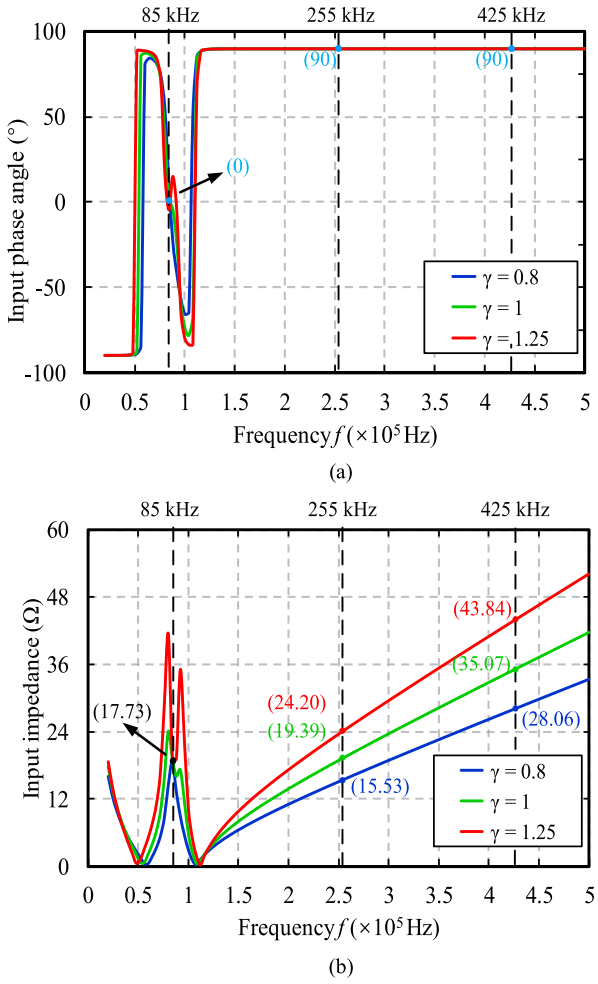

Fig. 5. Frequency-response characteristic of the DS-*LCC* topology under different γ values at 6.6-kW P_o. (a) Phase-frequency characteristic. (b) Amplitude-frequency characteristic.

As shown in Fig. 2, the secondary-side equivalent impedance is expressed as

$$\boldsymbol{Z}_s = j\omega L_s + \frac{1}{j\omega C_{f2}} + \frac{\frac{1}{j\omega C_{p2}}(j\omega L_2 + R_o)}{\frac{1}{j\omega C_{p2}} + j\omega L_2 + R_o}. \tag{20}$$

The reflected impedance, which is converted from the secondary side to the primary side can be obtained as

$$\boldsymbol{Z}_r = \frac{\omega^2 M^2}{Z_s}. \tag{21}$$

Then, the total input impedance of the DS-*LCC* topology can be attained as

$$\boldsymbol{Z}_{in} = j\omega L_1 + \frac{\frac{1}{j\omega C_{p1}}\left(j\omega L_p + \frac{1}{j\omega C_{f1}} + \boldsymbol{Z}_r\right)}{j\omega L_p + \frac{1}{j\omega C_{f1}} + \boldsymbol{Z}_r + \frac{1}{j\omega C_{p1}}}. \tag{22}$$

By substituting (18) and (19) in (22), and employing the parameters listed in Tables I and II, the amplitudes and phase angles of $\boldsymbol{Z}_{\rm in}$ under different γ values at 6.6-kW output power are calculated, as shown in Fig. 5. Because the FBI output voltage $\boldsymbol{U}_{\rm AB}$ consists only of odd harmonics, and the harmonic amplitudes above the fifth order are very small; therefore, only the fundamental (85 kHz), third (255 kHz), and fifth (425 kHz) harmonics are considered here. Fig. 5(a) shows that the ZPA can always be implemented at the specified resonant frequency (85 kHz) regardless of γ. There is a 90° input phase angle at both the third and fifth harmonics, indicating that only a reactive power is produced by the high-order harmonics.

For a more direct description of the HHS performance, two variables are defined as follows:

$$\xi_{1-3} = \frac{Z_{\rm in-1st}}{Z_{\rm in-3rd}} \tag{23}$$

$$\xi_{1-5} = \frac{Z_{\rm in-1st}}{Z_{\rm in-5th}}. \tag{24}$$

Among the above equations, $Z_{\rm in-1st}$, $Z_{\rm in-3rd}$, and $Z_{\rm in-5th}$ are the impedance amplitudes corresponding to the fundamental, third, and fifth harmonics, respectively; and ξ_{1-3} and ξ_{1-5} represent the impedance amplitude ratios between the fundamental harmonic and the high-order harmonics. As shown in Fig. 5(b), regardless of γ, $Z_{\rm in-1st}$ is the same at the resonant frequency. Therefore, it is apparent that smaller ξ_{1-3} and ξ_{1-5} values indicate better HHS performance. Thus, from Fig. 5(b), we can conclude that a larger γ value is better for the HHS.

In addition, to verify the above analysis, under the same calculation conditions as above, comparative simulations were performed using the PSIM 9.1 software, as shown in Fig. 6. Furthermore, the fast Fourier transform tool was used to analyze the input current $I_{\rm in}$ (I_{L1}). The fundamental harmonic amplitudes of $I_{\rm in}$ are almost unchanged, whereas those of the third and fifth harmonics decrease as γ increases. Hence, for a higher HHS performance, the selected γ value should be as large as possible.

D. Power Loss Analysis

As discussed in Section II-B, both I_p and I_s can be flexibly adjusted by varying γ, while the system parameters are held constant. Because the variations in I_p and I_s can generate significant effects on the power loss (system efficiency), the influence of γ on the system efficiency will be discussed here.

In the WPT system, the total power loss includes losses such as the core loss and copper loss of the LCT and the two compensation inductors, switching loss of the inverter, diode loss of the rectifier, capacitor loss, and some other stray loss [31]. Hence, it is difficult to predict the system efficiency precisely using a qualitative relation. However, based on the previous analysis, wherein the resonant network of the DS-*LCC* is reconfigured by changing γ, the system parameters, such as $U_{\rm AB}$, f_0, $I_{\rm in}$, and $I_{\rm o,}$ are theoretically identical, indicating that the losses of the inverter and rectifier are nearly the same under different γ values. In contrast, the number of turns of L_1 and L_2 vary with γ, namely, their ESRs may be different. Nevertheless, compared with the ESRs of L_p and L_s, those of L_1 and L_2 are much smaller. Moreover, the inductance value of an inductor is normally very sensitive to variations in its number of turns, while γ cannot change much, owing to the rated I_p and I_s. Therefore, the ESR

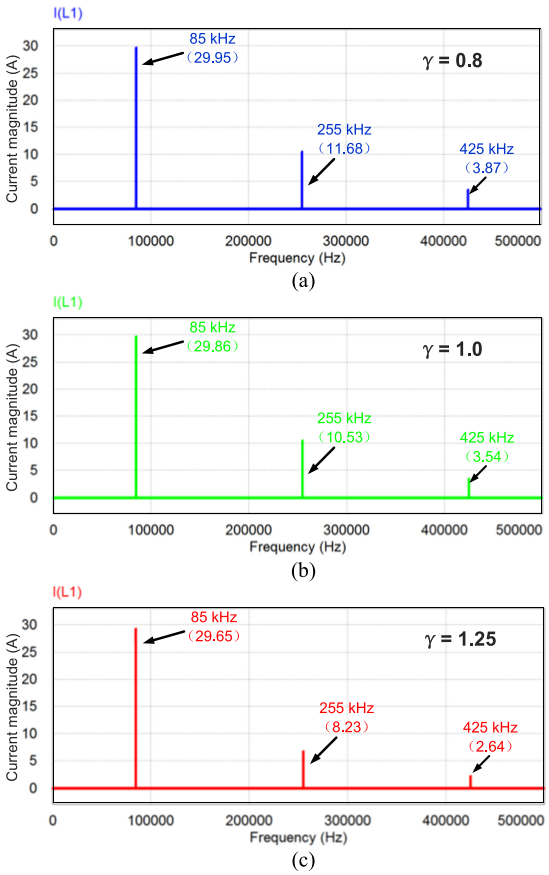

Fig. 6. PSIM simulation results of $I_{\rm in}$ (I_{L1}) harmonic under different γ values at 6.6-kW P_o. (a) $\gamma = 0.8$. (b) $\gamma = 1.0$. (c) $\gamma = 1.25$.

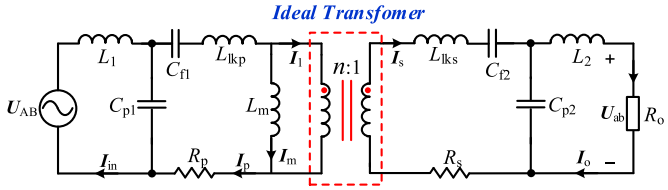

Fig. 7. Transformer equivalent model-based analytical circuit of the DS-*LCC* compensation topology.

variations of L_1 and L_2 can be ignored. Considering capacitor loss and stray loss, their contributions to the total losses are generally very small, and their difference is not evident at a constant P_o. Hence, these are also neglected here. Therefore, when γ changes, the variation trend of the efficiency can be indirectly predicted through the comparison and analysis of the LCT loss under different γ values.

Therefore, the total loss ($P_{\rm LCT}$) of the LCT can be divided into two parts: the core loss $P_{\rm Core}$, and copper loss P_{Cu}. Among these, $P_{\rm Core}$ mainly exists in the magnetic plates, whereas P_{Cu} mainly exists in the coils. Normally, $P_{\rm LCT}$ can be expressed as

$$P_{\rm LCT} = P_{\rm Core} + P_{\rm Cu}. \tag{25}$$

The mutual-inductance model of the LCT shown in Fig. 2 is replaced by a standard transformer model shown in Fig. 7,

TABLE III
ESSENTIAL PARAMETERS OF THE LCT TRANSFORMER MODEL

Symbols	Parameters	Values
n	Turn ratio	0.889
k	Coupling coefficient	0.164
M	Mutual inductance	6.54 μH
$L_{\rm m}$	Magnetizing inductance	5.82 μH
$L_{\rm lkp}$	Primary leakage inductance	31.18 μH
$L_{\rm lks}$	Secondary leakage inductance	32.64 μH
$R_{\rm p}$	Primary coil DC ESR	13.9 mΩ
$R_{\rm s}$	Secondary coil DC ESR	23.9 mΩ

which is more convenient for loss calculations. Based on the transformer theory, the two analytical models are equivalent, and their relational expressions can be derived as follows:

$$\begin{cases} n = \sqrt{L_p/L_s} \\ L_m = nM \\ L_{\rm lkp} = L_p - L_m \\ L_{\rm lks} = L_s - L_m/n^2 \end{cases} \tag{26}$$

where n is the turn ratio of the LCT; L_m is the magnetizing inductance, which is reflected from the secondary side to the primary side; and $L_{\rm lkp}$ and $L_{\rm lks}$ are the leakage inductances of the primary and secondary coils, respectively. By utilizing the system parameters listed in Table I, the transformer model parameters of the LCT are calculated using (26) and are listed in Table III. Generally, the total copper loss P_{Cu} can be expressed as

$$P_{\rm Cu} = {I_p}^2 R_p' + {I_s}^2 R_s' \tag{27}$$

where $R_p{}'$ and $R_s{}'$ in (27) are the ac ESRs of the coils, and R_p and R_s listed in Table III are the dc ESRs of the coils. Generally, while calculating P_{Cu}, the ac ESRs of the coils are considered more, owing to the skin and proximity effects which are affected by high frequency and generate additional ac winding loss. Although the litz wire, which consists of many copper strands, can be applied to reduce these two effects, the improvement is limited for a high-power WPT application. Therefore, for a more accurate calculation of P_{Cu}, a modified Dowell's equation is used here to determine the ac ESRs of the coils, $R_{\rm AC}$, as reported in [32]; thus, the following equation is obtained:

$$R_{AC} = R_{\rm DC}\beta \left[\frac{\sin h(2\beta) + \sin(2\beta)}{\cos h(2\beta) - \cos(2\beta)} + \frac{1.9({N_t}^2 - 1)}{3} \frac{\sin h(\beta) - \sin(\beta)}{\cos h(\beta) + \cos(\beta)} \right] \tag{28}$$

where $R_{\rm DC}$ is the dc ESRs of the coils, which can be directly measured, h is the diameter of the litz wire, $N_{\rm t}$ is the total effective number of copper strands of the coil, and β is the skin depth per unit diameter of the litz wire. The detailed calculation principle of these parameters can be found in [32].

Fig. 8 shows the three-dimensional (3-D) geometric structure of the LCT, which is designed according to the WPT 2 power class of SAE J2954 recommended practice, and its detailed dimensions are listed in Table IV. By applying (28), the ac ESRs, $R_p{}'$ and $R_s{}'$ are calculated to be 35.2 and 49.2 mΩ,

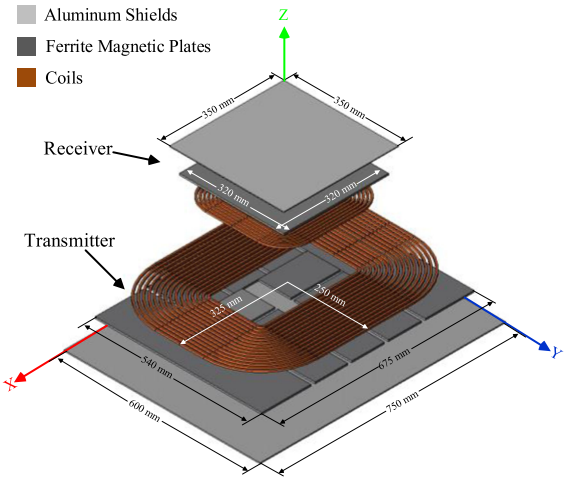

Fig. 8. 3-D geometric structure and dimensions of the designed LCT.

TABLE IV
DESIGNED DIMENSIONAL PARAMETERS OF THE LCT

Parameters	Values
Air gap distance	150 mm
Turns per coil	N_p: 15, N_s: 17
Primary coil dimensions	650 mm × 500 mm × 5.2 mm (0.12 mm/825), N_1[1]=1, ρ_1[2]= 11.6 mm
Primary ferrite plate dimensions	675 mm × 540 mm × 5 mm
Primary shield dimensions	750 mm × 600 mm × 1.5 mm
Secondary coil dimensions	320 mm × 320 mm × 4.6 mm (0.12 mm/600), N_2[1]=1, ρ_2[2]= 8.3 mm
Secondary ferrite plate dimensions	320 mm × 320 mm × 5 mm
Primary shield dimensions	350 mm × 350 mm × 1.5 mm

[1]Number of coil layers.
[2]Center distance of the adjacent litz wires.

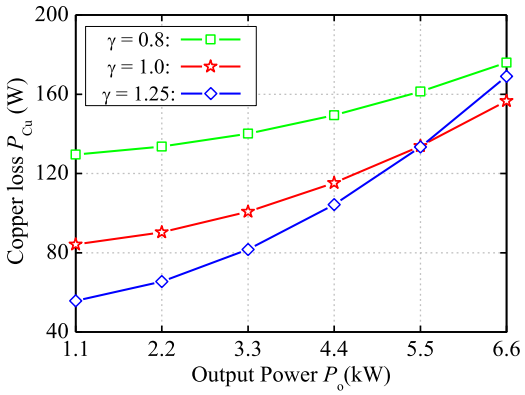

Fig. 9. Calculated P_{Cu} versus P_o under different γ values.

respectively, by using the parameters in Tables III and IV. Using the parameters listed in Tables I and II, the variations of P_{Cu} with P_o were calculated using (27) for different γ values, as shown in Fig. 9. We can see that P_{Cu} increases as P_o increases, regardless of γ. When P_o is small, P_{Cu} is lower at larger γ values, but it increases more rapidly as P_o increases. In addition, the LCT is much different with the general transformer, wherein the LCT has a large leakage magnetic flux (MF). Therefore,

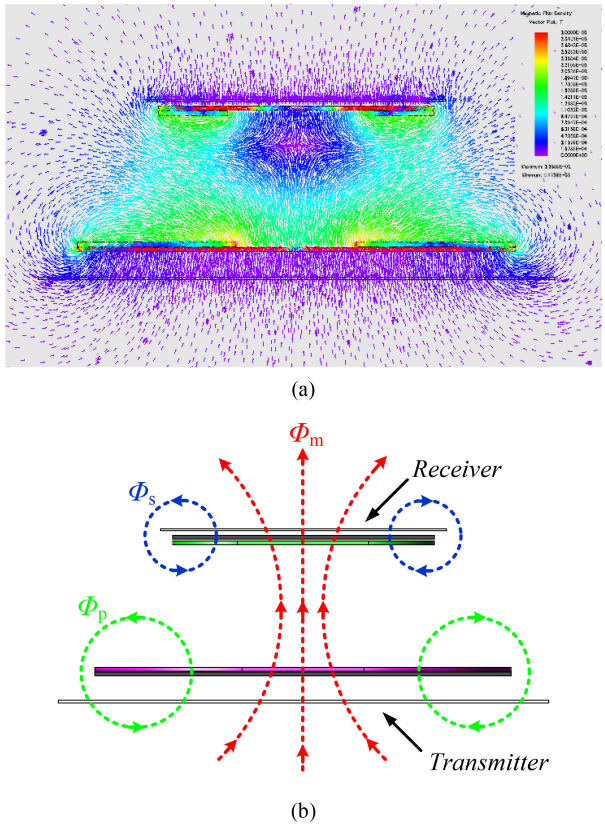

Fig. 10. MF distribution of the LCT in the DS-*LCC* topology. (a) FEM simulation diagram. (b) Simplified illustration.

ferrite is widely utilized to intensify the magnetic field. Fig. 10(a) shows the MF distribution of the LCT, which is simulated by the JMAG finite element analysis (FEM) tool; the simulation parameters are consistent with the parameters listed in Table IV. The MF distribution of the LCT can be simplified according to the magnetic theory, as shown in Fig. 10(b), where $\boldsymbol{\Phi}_m$ is the mutual MF generated by L_m, and $\boldsymbol{\Phi}_p$ and $\boldsymbol{\Phi}_s$ are the leakage MFs of the primary and secondary coils, respectively. The total MF, which passes through each coil, can be expressed as

$$\begin{cases} \boldsymbol{\Phi}_1 = \boldsymbol{\Phi}_p + \boldsymbol{\Phi}_m \\ \boldsymbol{\Phi}_2 = \boldsymbol{\Phi}_s + \boldsymbol{\Phi}_m. \end{cases} \tag{29}$$

Generally, if an ac current $\boldsymbol{I}$ flows into a coil with N turns and the inductance is L, then according to the law of electromagnetic induction, the following equation can be used:

$$L\boldsymbol{I} = N\boldsymbol{\Phi} \tag{30}$$

where $\boldsymbol{\Phi}$ is the MF through the coil. As shown in Fig. 7, by combining (26), (29), and (30) and according to Kirchhoff's voltage and current laws, (29) can be modified as

$$\begin{cases} \boldsymbol{\Phi}_1 = \frac{L_{lkp}\boldsymbol{I}_p}{N_1} + \frac{L_m\boldsymbol{I}_m}{N_1} \\ \boldsymbol{\Phi}_2 = \frac{L_{lks}\boldsymbol{I}_s}{N_2} + \frac{L_m\boldsymbol{I}_m}{N_1}. \end{cases} \tag{31}$$

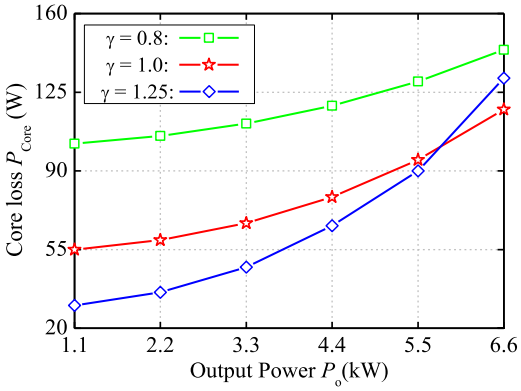

Fig. 11. Calculated P_{Core} versus P_o under different γ values.

Using the Steinmetz equation and substituting (31) therein, the total core loss P_{Core} can be calculated as

$$P_{\mathrm{Core}} = k_1 f^{\alpha}\left(\Phi_{1\max}{}^{\beta} S_1{}^{(1-\beta)} h_1 + \Phi_{2\max}{}^{\beta} S_2{}^{(1-\beta)} h_2\right) \tag{32}$$

where k_1, α, and β are the empirical coefficients, which can be obtained from the ferrite datasheet: as the PC95 ferrite was used in this article, these values are 0.074, 1.43, and 2.85, respectively; $\Phi_{1\max}$ and $\Phi_{2\max}$ are the peak values of $\mathbf{\Phi}_1$ and $\mathbf{\Phi}_2$, respectively; and h_1 (h_2) and S_1 (S_2) are the thickness and sectional area of the primary (secondary) ferrite plates, respectively. By combining (31) and (32) and using the parameters provided earlier, the variations of P_{Core} with P_o are calculated for different γ values, as shown in Fig. 11. A variation trend is similar to that of P_{Cu}, i.e., P_{Core} increases as P_o increases under different γ values; moreover, at low P_o, P_{Core} corresponding to different γ varies greatly, and although P_{Core} under a larger γ is rather small, it increases rapidly as P_o increases.

Based on the above analysis, P_{LCT} is calculated under the continuous variations of γ and P_o, as shown in Fig. 12, and the following observations are made: as P_o increases, the overall variation trend of P_{LCT} is consistent with that of P_{Cu} and P_{Core}. When P_o is low, P_{LCT} increases monotonically as γ decreases.

However, at a high P_o, as γ varies from 0.5 to 1.75, P_{LCT} first decreases and then increases, while a low P_{LCT} is achieved at intermediate γ.

To visualize the P_{LCT}, the contour line of P_{LCT} is shown in Fig. 12(b). At smaller γ values, P_{LCT} is always high regardless of the P_o; whereas, when γ is large, although a low P_{LCT} can be obtained at a low P_o, it is very high when P_o is large. Nevertheless, within the central region, when γ is larger than 0.95, as γ increases, the P_{LCT} steadily falls at the low P_o values, while it steadily rises at high P_o values. As a result, an appropriate γ value should be selected to satisfy the tradeoff between high efficiency at high P_o and that at low P_o.

III. Efficiency Optimization-Based Asymmetric Tuning Procedure for the DS-LCC Topology

Fig. 12 presents a wide range of γ values; however, according to the analysis in Section II-B, the possible range of γ is limited

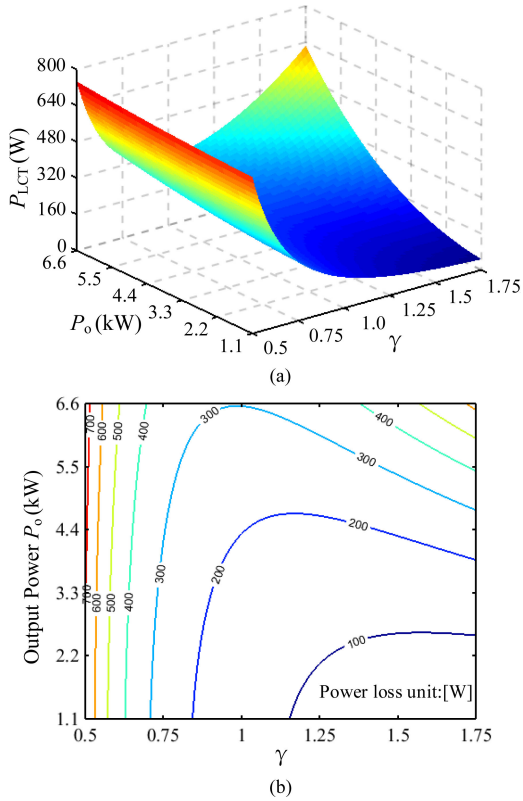

Fig. 12. Power loss analysis of the LCT. (a) Calculated P_{LCT} versus P_o and γ. (b) Contour line of P_{LCT}.

by the rated I_p and I_s, which are determined by the thicknesses of the primary and secondary coils, respectively. In this article, as listed in Table IV, the thicknesses of the coils are 5.2 mm (AWG 4) and 4.6 mm (AWG 5). Then, the rated I_p and I_s are 60 and 47 A, respectively, as per the litz wire datasheet. Finally, based on the rated coil currents and Fig. 4, we determine the possible range of γ as 0.8–1.26.

Within the feasible γ region, efficiency optimization is favored at high P_o for smaller γ values and at low P_o for larger γ values. Hence, it is difficult to select a γ value for efficiency optimization under the overall P_o. However, by combining Figs. (9), (11), and (12), under different γ values, it is evident that the difference in P_{LCT} at low P_o is much higher than that at high P_o, indicating that the efficiency difference between the different γ values is much more distinct at a lower P_o. In addition, during the CC and CV hybrid charging process, which is widely used in EV applications, the charging time at small or medium P_o is much longer than that at high P_o. Considering the weighting of the P_{LCT} difference under different P_o values, a power loss factor ζ is defined as follows:

$$\zeta = \sum_{i=1}^{k} \frac{P_{\mathrm{LCT}-i}}{P_{o-i}} = \frac{P_{\mathrm{LCT}-1.1}}{1100} + \frac{P_{\mathrm{LCT}-2.2}}{2200} + \frac{P_{\mathrm{LCT}-3.3}}{3300} + \frac{P_{\mathrm{LCT}-4.4}}{4400} + \frac{P_{\mathrm{LCT}-5.5}}{5500} + \frac{P_{\mathrm{LCT}-6.6}}{6600} \tag{33}$$

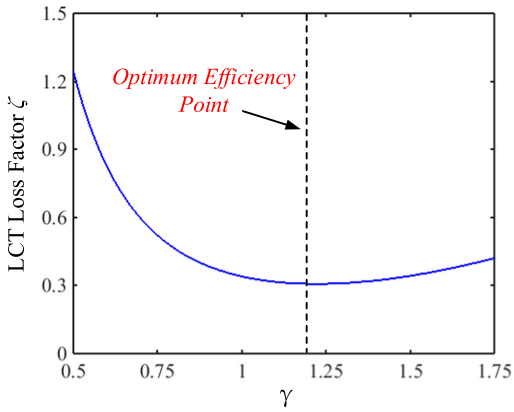

Fig. 13. Calculated power loss factor ζ versus γ.

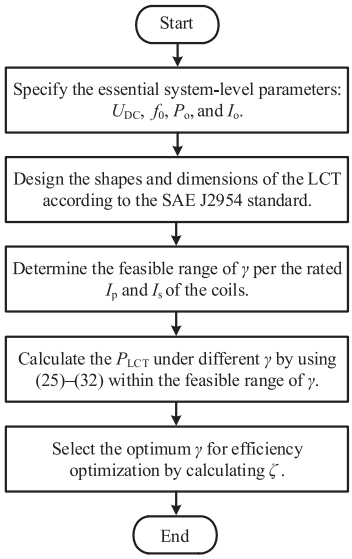

Fig. 14. Flowchart of the proposed efficiency optimization-based asymmetric tuning procedure for the DS-LCC topology.

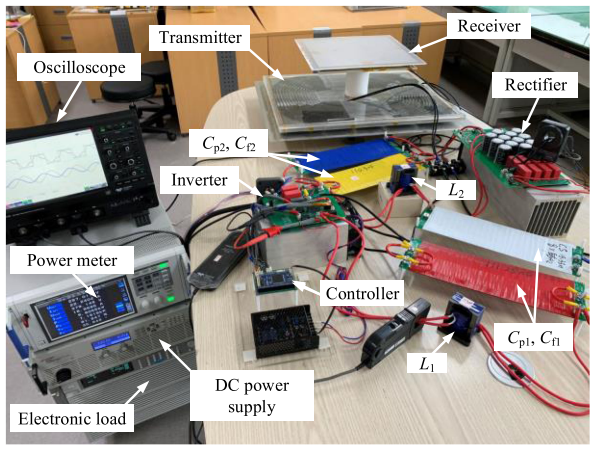

Fig. 15. Experimental prototype of the DS-*LCC* WPT system.

TABLE V
MEASURED LCT PARAMETERS

Symbols	Practical Values
k	0.163
L_p	40.4 μH
L_s	39.8 μH
R_p	13.9 mΩ
R_s	23.9 mΩ

TABLE VI
PRACTICAL RECONFIGURABLE PARAMETERS OF THE DS-*LCC* COMPENSATION TOPOLOGY

Parameters	Values				
	$\gamma = 0.82$	$\gamma = 0.9$	$\gamma = 1.0$	$\gamma = 1.11$	$\gamma = 1.22$
L_1 (μH)	10.82	11.83	13.27	14.81	16.03
L_2 (μH)	16.03	14.81	13.18	11.83	10.82
C_{p1} (nF)	323.12	294.55	265.31	238.72	217.71
C_{p2} (nF)	217.71	238.72	265.06	294.55	323.12
C_{f1} (nF)	120.41	124.86	131.42	139.61	147.92
C_{f2} (nF)	147.92	139.61	130.78	124.86	120.41

where P_{o-i} indicates the different output power, and P_{LCT-i} is the corresponding total power loss of the LCT. When the other parameters remain unchanged, the value of P_{LCT-i} varies only with γ. Therefore, ζ is calculated at different γ values, as shown in Fig. 13. ζ does not vary monotonically with γ and is lowest at $\gamma = 1.2$. Thus, this point is considered as the optimum selection, which provides a better efficiency tradeoff in the overall P_o range.

It should be noted that the optimum γ may vary with the different parameters of the WPT system. Thus, based on the above selection principles, the general asymmetric tuning procedure of the DS-*LCC* topology for efficiency optimization is summarized as shown in Fig. 14.

IV. EXPERIMENTAL VERIFICATION

To verify the above theoretical analysis and comparison, a 6.6-kW experimental setup of the DS-*LCC* WPT system was configured, as shown in Fig. 15. In this setup, the main system parameters such as U_{DC}, f_0, and I_b are consistent with those listed in Table I. The LCT is designed and manufactured according to the parameters listed in Table IV, which fulfill the SAE J2954 recommended practice. The practical LCT parameters were measured, as listed in Table V.

Four SiC MOSFETs C3M0030090K and four Schottky diodes IDW20G120C5B are selected as the FBI and BR, respectively. A DSP TMS320F28335 was used to control the WPT system. In the feasible γ region (0.8–1.26), except for the conventional symmetric setting at $\gamma = 1.0$, two sets of γ values with reciprocal relationships were selected for reducing the workload of the resonant network reconstructions. Their practical parameters are listed in Table VI, and the deviation between the designed and practical parameters was found to be less than 1%. The ferrite core PC95PQ60/42-Z was used to build L_1 and L_2. To obtain more accurate compensation inductances, their values were adjusted by modifying the number of turns and air gap under different γ values. The practical parameters of the

TABLE VII
PRACTICAL PARAMETERS OF COMPENSATION INDUCTORS

Inductances (μH)	Values				
	10.82	11.83	13.27	14.81	16.03
Number of turns	7.5[1]	9.0	11.5[1]	15.5[1]	17.0
DC ESR (mΩ)	8.1	9.4	11.8	15.3	16.5
Air gap (mm)	3.4	3.4	3.5	3.4	3.6

[1]0.5 indicates a half-turn number.

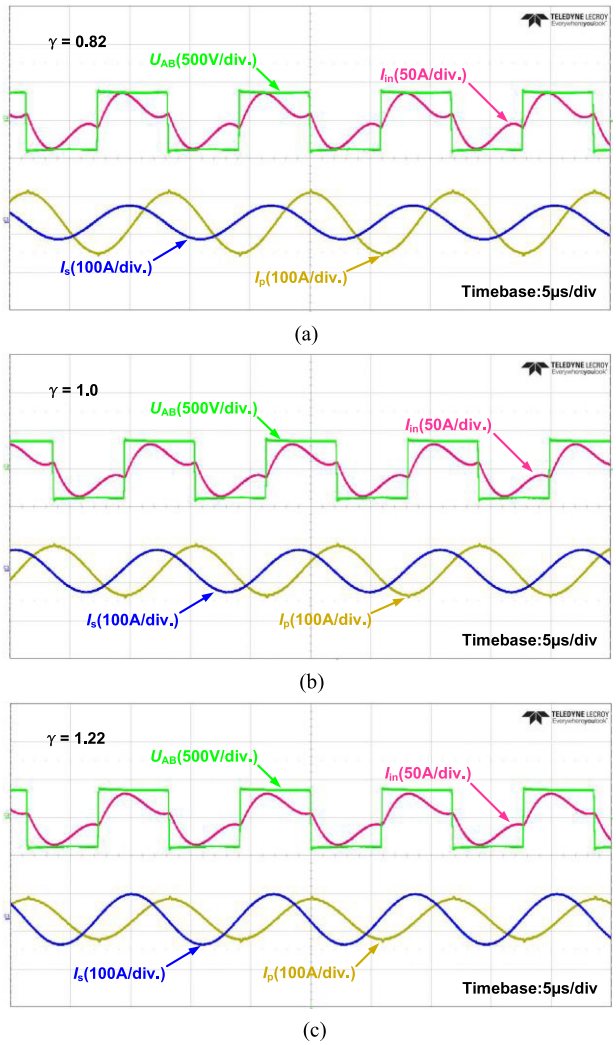

Fig. 16. Waveforms of $\boldsymbol{U}_{\mathrm{AB}}$, $\boldsymbol{I}_{\mathrm{in}}$, $\boldsymbol{I}_p$, and $\boldsymbol{I}_s$ under different γ values at 6.6-kW P_o. (a) $\gamma = 0.82$. (b) $\gamma = 1.0$. (c) $\gamma = 1.22$.

compensation inductors are listed in Table VII. In addition, The PCB-type compensation capacitor tanks consist of the series–parallel connections of the SMD chip ceramic capacitor C1812C222JDGAC7800.

Using the abovementioned experimental setup, and considering that all system parameters except γ are held constant, the comparative experiments were conducted under the different γ values listed in Table VI. Fig. 16 shows the waveforms of $\boldsymbol{U}_{\mathrm{AB}}$, $\boldsymbol{I}_{\mathrm{in}}$, $\boldsymbol{I}_p$, and $\boldsymbol{I}_s$ when P_o is 6.6 kW, $\boldsymbol{U}_{\mathrm{AB}}$ is a constant, and zero-voltage switching (ZVS) is implemented

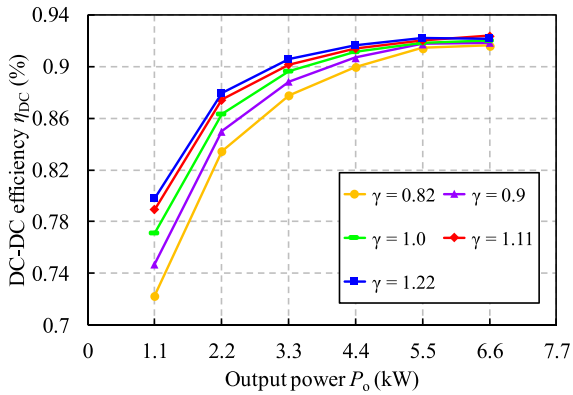

Fig. 17. Measured overall system efficiency versus P_o under different γ values.

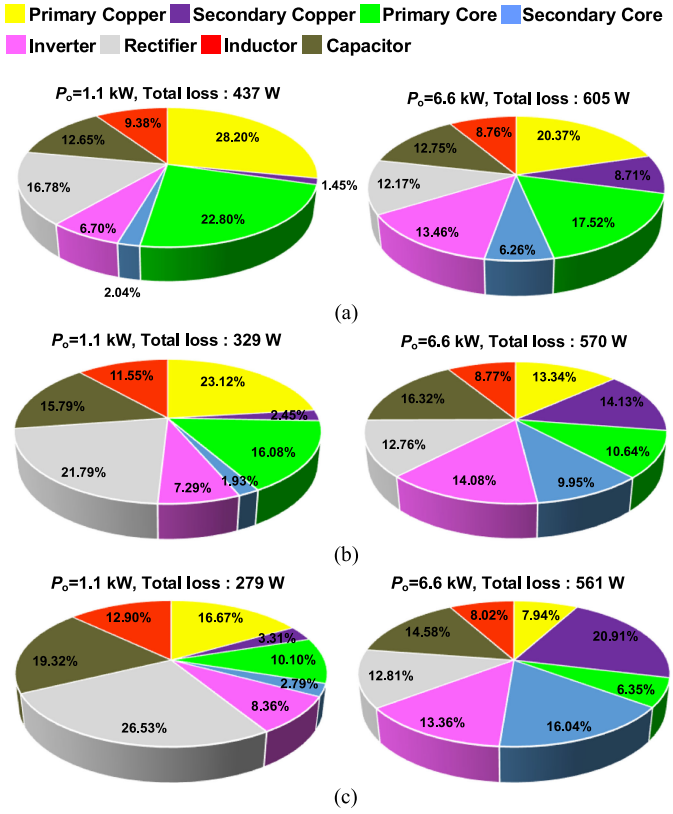

Fig. 18. Power loss distribution of the DS-LCC WPT system under different γ and P_o values. (a) $\gamma = 0.82$. (b) $\gamma = 1.0$. (c) $\gamma = 1.22$.

in all cases. As γ increases, $\boldsymbol{I}_p$ decreases while $\boldsymbol{I}_s$ increases. The reason for the slight drop in $\boldsymbol{I}_{\mathrm{in}}$ is the variation in system efficiencies and the HHS performances under different γ values. As γ varies, the overall system efficiency η_{DC} is measured via a power meter under different P_o values, as shown in Fig. 17. Under light load conditions, a larger γ provides a higher η_{DC}, especially at $P_o = 1.1$ kW; the maximum η_{DC} is 79.83% at $\gamma = 1.22$; and the minimum η_{DC} is 72.29% at $\gamma = 0.82$. However, this trend of η_{DC} gradually decreases as P_o increases, and the η_{DC} values are almost identical at $P_o =$ 6.6 kW: at this value, the maximum η_{DC} is 92.39% at $\gamma = 1.11$, and the minimum η_{DC} is 91.64% at $\gamma = 0.82$. By comparing

$\gamma = 1.11$ and $\gamma = 1.22$, even at 1.1-kW P_o, there is only a slight increase in $\eta_{\rm DC}$, indicating that the uptrend of $\eta_{\rm DC}$ is almost saturated as γ increases. Meanwhile, at 6.6-kW P_o, the $\eta_{\rm DC}$ at $\gamma = 1.22$ is slightly lower than that at $\gamma = 1.11$, indicating that $\eta_{\rm DC}$ begins to drop as γ increases beyond $\gamma = 1.11$. As a result, $\gamma = 1.22$ is considered as the optimum ratio of L_1 and L_2, which is similar to the estimated optimum ratio above.

Furthermore, the system power losses were measured and calculated under different γ values, at $P_o = 1.1$ kW and 6.6 kW, respectively, as shown in Fig. 18. At 1.1-kW P_o, the primary copper loss and core loss decrease sharply as γ increases, while the difference between the secondary copper loss and core loss at different γ values can be neglected because these only account for a fraction of the $P_{\rm LCT}$. Meanwhile, at 6.6-kW P_o, there is a decrease in the primary copper loss and core loss as γ increases, while the secondary copper loss and core loss increase sharply. As a result, although the γ values are different, there is almost no difference in the $P_{\rm LCT}$ at a high P_o. Furthermore, the losses of the other parts are also similar under a same P_o. Because the CC output character of the DS-*LCC* topology, the rectifier losses under different γ are nearly identical regardless P_o. Thus, the experimental power loss distribution is almost consistent with the previous loss analysis.

V. Conclusion

In this article, a novel asymmetric parameter-tuning method is proposed for the DS-*LCC* WPT system to optimize efficiency over the entire output power range. Under the premise that the essential system-level parameters are established, the DS-*LCC* resonant network was reconstructed by changing the ratio of the compensation inductances. Thus, the primary and secondary coil currents can be adjusted to generate different system characteristics. Comprehensive comparisons and analyses under different combinations were conducted and an optimum inductance ratio was established with high efficiency as the primary objective. In addition, by accounting for the systematic differences, a general optimization efficiency-based tuning procedure for the DS-*LCC* system was presented. An experimental prototype with a 6.6-kW rated output power was configured to validate the reasonability of the proposed parameter-tuning method. Five different sets of compensation parameters were established to compare the efficiency. The results showed that, compared with the conventional symmetric tuning method, the proposed asymmetric tuning method effectively improves the system efficiency in the overall output power range.

References

[1] V. B. Vu, D. H. Tran, and W. Choi, "Implementation of the constant current and constant voltage charge of inductive power transfer systems with the double-sided LCC compensation topology for electric vehicle battery charge applications," *IEEE Trans. Power Electron.*, vol. 33, no. 9, pp. 7398–7410, Sep. 2018.

[2] Y. Chen, H. Zhang, S. Park, and D. Kim, "A switching hybrid LCC-S compensation topology for constant current/voltage EV wireless charging," *IEEE Access*, vol. 7, pp. 133924–133935, Sep. 2019.

[3] D. Patil, M. K. McDonough, J. M. Miller, B. Fahimi, and P. T. Balsara, "Wireless power transfer for vehicular applications: Overview and challenges," *IEEE Trans. Transp. Electrific.*, vol. 4, no. 1, pp. 3–37, Mar. 2018.

[4] Y. Yao, Y. Wang, X. Liu, F. Lin, and D. Xu, "A novel parameter tuning method for a double-sided LCL compensated WPT system with better comprehensive performance," *IEEE Trans. Power Electron.*, vol. 33, no. 10, pp. 8525–8536, Oct. 2018.

[5] K. Song *et al.*, "Constant current charging and maximum system efficiency tracking for wireless charging systems employing dual-side control," *IEEE Trans. Ind. Appl.*, vol. 56, no. 1, pp. 622–634, Jan. 2020.

[6] Z. Zhang, H. Pang, A. Georgiadis, and C. Cecati, "Wireless power transfer-an overview," *IEEE Trans. Ind. Electron.*, vol. 66, no. 2, pp. 1044–1058, Feb. 2019.

[7] S. Li and C. Mi, "Wireless power transfer for electric vehicle applications," *IEEE J. Emerg. Sel. Topics Power Electron.*, vol. 3, no. 1, pp. 4–17, Mar. 2015.

[8] W. Zhang, J. C. White, R. K. Malhan, and C. C. Mi, "Loosely coupled transformer coil design to minimize EMF radiation in concerned areas," *IEEE Trans. Veh. Technol.*, vol. 65, no. 6, pp. 4779–4789, Jun. 2016.

[9] M. Budhia, G. A. Covic, and J. T. Boys, "Design and optimization of circular magnetic structures for lumped inductive power transfer systems," *IEEE Trans. Power Electron.*, vol. 26, no. 11, pp. 3096–3108, Nov. 2011.

[10] Z. Pantic, B. Sanzhong, and S. Lukic, "ZCS LCC-compensated resonant inverter for inductive-power-transfer application," *IEEE Trans. Ind. Electron.*, vol. 58, no. 8, pp. 3500–3510, Aug. 2011.

[11] S. Samanta and A. K. Rathore, "Analysis and design of load independent ZPA operation for P/S, PS/S, P/SP, and PS/SP tank networks in IPT applications," *IEEE Trans. Power Electron.*, vol. 33, no. 8, pp. 6476–6482, Aug. 2018.

[12] J. Hou, Q. Chen, S.-C. Wong, and C. K. Tse, and X. Ruan, "Analysis and control of series/series-parallel compensated resonant converter for contactless power transfer," *IEEE J. Emerg. Sel. Topics Power Electron.*, vol. 3, no. 1, pp. 124–136, Mar. 2015.

[13] H. Li, J. Li, K. Wang, W. Chen, and Y. Xu, "A maximum efficiency point tracking control scheme for wireless power transfer systems using magnetic resonant coupling," *IEEE Trans. Power Electron.*, vol. 30, no. 7, pp. 3998–4008, Jul. 2015.

[14] X. Dai, X. Li, Y. Li, and P. Hu, "Maximum efficiency tracking for wireless power transfer systems with dynamic coupling coefficient estimation," *IEEE Trans. Power Electron.*, vol. 33, no. 6, pp. 5005–5015, Jun. 2018.

[15] W. Li, H. Zhao, J. Deng, S. Li, and C. Mi, "Comparison study on SS and double-sided LCC compensation topologies for EV/PHEV wireless chargers," *IEEE Trans. Veh. Technol.*, vol. 65, no. 6, pp. 4429–4439. Jun. 2016.

[16] W. Zhang, S. C. Wong, C. K. Tse, and Q. Chen, "Design for efficiency optimization and voltage controllability of series-series compensated inductive power transfer systems," *IEEE Trans. Power Electron.*, vol. 29, no. 1, pp. 191–200, Jan. 2014.

[17] Y. Chen, N. Yang, Q. Li, Z. He, and R. Mai, "New parameter tuning method for LCC/LCC compensated IPT system with constant voltage output based on LC resonance principles," *IET Power Electron.*, vol. 12, no. 10, pp. 2466–2474, Aug. 2011.

[18] J. Hou, Q. Chen, Z. Zhang, S.-C. Wong, and C. K. Tse, "Analysis of output current characteristics for higher order primary compensation in inductive power transfer systems," *IEEE Trans. Power Electron.*, vol. 33, no. 8, pp. 6807–6821, Aug. 2018.

[19] J. Lu, G. Zhu, H. Wang, F. Lu, J. Jiang, and C. C. Mi, "Sensitivity analysis of inductive power transfer systems With voltage-fed compensation topologies," *IEEE Trans. Veh. Technol.*, vol. 68, no. 5, pp. 4502–4513, Mar. 2019.

[20] F. Lu, H. Zhang, H. Hofmann, W. Su, and C. Mi, "A dual-coupled LCC compensated IPT system with a compact magnetic coupler," *IEEE Trans. Power Electron.*, vol. 33, no. 7, pp. 6391–6402, Jul. 2018.

[21] S. Li, W. Li, J. Deng, T. D. Nguyen, and C. Mi, "A double-sided LCC compensation network and its tuning method for wireless power transfer," *IEEE Trans. Veh. Technol.*, vol. 64, no. 6, pp. 2261–2273, Jun. 2015.

[22] W. Li, H. Zhao, J. Deng, T. Kan, and C. Mi, "Integrated LCC compensation topology for wireless charger in electric and plug-in electric vehicles," *IEEE Trans. Ind. Electron.*, vol. 62, no. 7, pp. 4215–4225, Jul. 2015.

[23] S. Zhou and C. Mi, "Multi-paralleled LCC reactive power compensation networks and their tuning method for electric vehicle dynamic wireless charging," *IEEE Trans. Ind. Electron.*, vol. 63, no. 10, pp. 6546–6556, Oct. 2016.

[24] S. Zou *et al.*, "Secondary active rectifier Control Scheme for a Wireless power Transfer System with double-sided LCC compensation topology," in *Proc. 42th Annu. Conf. IEEE Ind. Electron. Soc.*, Washington, DC, USA, Oct. 2018, pp. 2145–2150.

[25] F. Lu, H. Hofmann, J. Deng, and C. Mi, "Output power and efficiency sensitivity to circuit parameter variations in double-sided LCC-compensated wireless power transfer system," in *Proc. IEEE Appl. Power Electr. Conf.*, Charlotte, VA, USA, Mar. 2015, pp. 507–601.
[26] K. Takeda and T. Koseki, "Analytical investigation on asymmetric LCC compensation circuit for trade-off between high efficiency and power," in *Proc. Int. Power Electron. Conf.*, 2018, pp. 2309–2316.
[27] C. Liao, J. Li, and S. Li, "Design of LCC impedance matching circuit for wireless power transfer system under rectifier load," *CPSS Trans. Power Electron. Appl.*, vol. 2, no. 3, pp. 237–245, Sep. 2017.
[28] R. L. Steigerwald, "A comparison of half-bridge resonant converter topologies," *IEEE Trans. Power Electron.*, vol. 3, no. 2, pp. 174–182, Apr. 1988.
[29] SAE Wireless Power Transfer for Light-Duty Plug-In and Electric Vehicles and Alignment Methodology, SAE Standard J2954, May 2016.
[30] H. Zeng, S. Yang, and F. Z. Peng, "Design consideration and comparison of wireless power transfer via harmonic current," *IEEE Trans. Power Electron.*, vol. 32, no. 8, pp. 5943–5952, Aug. 2017.
[31] H. Wenshan, Y. Lingsong, L. Zhiwei, and Y. Hui, ''Loss analysis and improvement of all parts of magnetic resonant wireless power transfer system," in *Proc. Chin. Autom. Congr.*, Nov. 2015, pp. 2251–2256.
[32] R. P. Wojda and M. K. Kazimierczuk, "Winding resistance of litz-wire and multi-strand inductors," *IET Power Electron.*, vol. 5, no. 2, pp. 257–268, Feb. 2012.

Yafei Chen (Student Member, IEEE) received the B.S. degree in electronic information engineering from Southwest Jiaotong University, Chengdu, China, in 2012, and the M.S. degree in control theory and control engineering from the Qingdao University of Science and Technology, Qingdao, China, in 2016. He is currently working toward the Ph.D. degree in electrical engineering with Chonnam National University, Gwangju, South Korea.

His research interests include wireless power transfer for EVs and UAVs, topology, modeling and control of power converters, and applications for battery charger converters.

Hailong Zhang (Student Member, IEEE) received the B.S. degree in electronic engineering and automation from China Petroleum University, Dongying, China, in 2013, and the M.S. degree in control theory and control engineering from the Qingdao University of Science and Technology, Qingdao, China, in 2016. He is currently working toward the Ph.D. degree in electrical engineering with Chonnam National University, Gwangju, South Korea.

His research interests include wireless power transfer system for UAVs, power conversion system for EVs, and renewable energy storage systems.

Chang-Su Shin received the B.S. degree in information and communication engineering from Mokpo Maritime University, Mokpo, South Korea, in 2019. He is currently working toward the M.S. degree in electrical engineering with Chonnam National University, Gwangju, South Korea.

His research interests include wireless power transfer system for EVs, UAVs, and AGVs.

Cheol-Hee Jo received the B.S. degree in electrical engineering from Chonnam National University, Gwangju, South Korea, in 2019. He is currently working toward the M.S. degree in electrical engineering with Chonnam National University.

His research interests include power conditioning system dc–dc converters for renewable energy, battery chargers for hybrid electric vehicles/electric vehicles, and wireless power transfer for EVs and UAVs.

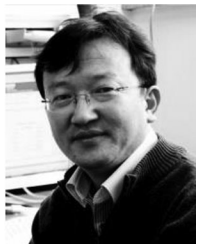

Sung-Jun Park (Member, IEEE) received the B.S., M.S., and Ph.D. degrees in electrical engineering, and the Ph.D. degree in mechanical engineering from Pusan National University, Busan, South Korea, in 1991, 1993, 1996, and 2002, respectively.

From 1996 to 2000, he was an Assistant Professor with the Department of Electrical Engineering, Koje College, Koje, South Korea. From 2000 to 2003, he was an Assistant Professor with the Department of Electrical Engineering, Tong-Myong College, Busan. Since 2003, he has been a Professor with the Department of Electrical Engineering, Chonnam National University, Gwangju, South Korea. His research interests include power electronics, motor control, mechatronics, and micromachine automation.

Dong-Hee Kim (Member, IEEE) received the B.S., M.S., and Ph.D. degrees in electrical engineering from Sungkyunkwan University, Suwon, South Korea, in 2009, 2011, and 2015, respectively.

From 2015 to 2016, he was a Postdoc Researcher with Sunkyunkwan University. Since 2016, he has been a part-time Lecturer with Daejin University, Pocheon, South Korea, and Shandong University of Technology, Shandong, China, respectively. From September 2016 to August 2017, he was an Assistant Professor with Tongmyong University, Busan, South Korea. In September 2017, he joined Chonnam National University, Gwangju, South Korea, as an Assistant Professor. His research interests include power conditioning system dc–dc converters for renewable energy, battery chargers for hybrid electric vehicles/electric vehicles, and wireless power transfer for EVs and UAVs.